

LA-UR-15-24599

Approved for public release; distribution is unlimited.

Title: Fully Autonomous Multiplet Event Detection: Application to
Local-Distance Monitoring of Blood Falls Seismicity

Author(s): Carmichael, Joshua Daniel
Carr, Christina
Pettit, Erin C.

Intended for: Report

Issued: 2015-06-18

Disclaimer:

Los Alamos National Laboratory, an affirmative action/equal opportunity employer, is operated by the Los Alamos National Security, LLC for the National Nuclear Security Administration of the U.S. Department of Energy under contract DE-AC52-06NA25396. By approving this article, the publisher recognizes that the U.S. Government retains nonexclusive, royalty-free license to publish or reproduce the published form of this contribution, or to allow others to do so, for U.S. Government purposes. Los Alamos National Laboratory requests that the publisher identify this article as work performed under the auspices of the U.S. Department of Energy. Los Alamos National Laboratory strongly supports academic freedom and a researcher's right to publish; as an institution, however, the Laboratory does not endorse the viewpoint of a publication or guarantee its technical correctness.

Title

Fully Autonomous Multiplet Event Detection: Application to Local-Distance Monitoring of Blood Falls Seismicity.

Authors

Joshua D Carmichael¹, Christina Carr², Erin C. Pettit²

Abstract

We apply a fully autonomous icequake detection methodology to a single day of high-sample rate (200 Hz) seismic network data recorded from the terminus of Taylor Glacier, ANT that temporally coincided with a brine release episode near Blood Falls (May 13, 2014). We demonstrate a statistically validated procedure to assemble waveforms triggered by icequakes into populations of clusters linked by intra-event waveform similarity. Our processing methodology implements a noise-adaptive power detector coupled with a complete-linkage clustering algorithm and noise-adaptive correlation detector. This detector-chain reveals a population of 20 multiplet sequences that includes ~150 icequakes and produces zero false alarms on the concurrent, diurnally variable noise. Our results are very promising for identifying changes in background seismicity associated with the presence or absence of brine release episodes. We thereby suggest that our methodology could be applied to longer time periods to establish a brine-release monitoring program for Blood Falls that is based on icequake detections.

1. Introduction

Blood Falls is a release of hypersaline, subglacial brine at the surface of the Taylor Glacier in the McMurdo Dry Valleys that provides an accessible portal into an Antarctic subglacial ecosystem. Taylor Glacier is a cold-based glacier that overlies sedimentary bedrock and a preglacial marine deposit providing the ultimate source for a basal brine system. Little is known about the origin of this brine, the amount of time it has been sealed below Taylor Glacier, or the extent to which the brine is altered as it makes its way to the surface at Blood Falls or what triggers its episodic release exclusively at Blood Falls. Recent geomicrobiological analysis of the outflow has revealed a unique community of marine organisms that persist by cycling iron and sulfur compounds for growth. Little is known about the hydrology of the glacier, the physical structure of the subglacial habitat, or the mechanism of brine release to the surface.

There are several motivating questions relating the seismicity of Taylor Glacier to englacial or subglacial fluid flow. Previous geophysical work on Taylor Glacier has related surficial melt input to a crack near Blood Falls, at a time when no brine release was observed. Immediate, further work on Taylor Glacier seismicity seeks to answer the following two questions: (1) “What is the seismic expression of brine outflow events from Blood Falls?” and (2) “How does seasonal seismicity related to summer melt events compare with seismicity associated with brine outflow?”

¹ Ground Based Nuclear Detonation Detection Group, Los Alamos National Laboratory, Los Alamos, NM, 87544

² Geophysical Institute, University of Alaska Fairbanks, Fairbanks AK 99775

Mission

To address our first objective, we determine if brine release episodes from Taylor Glacier, ANT (Figure 1) have detectable seismic signatures. A positive identification of such signatures requires that icequakes attributed to a documented brine release is distinguishable from any expected background seismicity in timing and/or location. To determine if such signatures exist, we first searched for repeatable icequakes indicative of active collocated events on days that include known discharge events (e.g., Figure 2). We propose to then search for these same, repetitive icequakes (multiplets) on days with no known discharge events. We will accept the hypothesis that icequakes spatiotemporally located with brine release episodes are strong indicators for brine seep unrest if these icequakes are not observed during relative quiescence. We will reject this hypothesis if such release points are associated with spatially coincident active seismicity, without any observable surface expression.

Here, we demonstrate an autonomous multiplet detector using a single day of seismic network data recorded on day of year (DOY) 133, 2014. Our immediate goal is to demonstrate a capability to evaluate repeating seismicity from Blood Falls rapidly and thereby enable more focused analyses on the icequake locations and source magnitudes in the presence and absence of coincident, brine discharge events. Future work will then be devoted to a fully addressing the competing hypotheses (stated above).

2. Data

Geophysical data were collected from Taylor Glacier (-77.721, +162.266) during 2013-2015 and included GPS, seismic, ground penetrating radar, time-lapse imagery, and interferometric datasets. The near-terminus region, in particular, was instrumented with three triaxial geophones (L-22 geophones) during the local summer of 2013 (Figure 1). One of the three sensors (JESS) was installed within ~1 m deep ice pit, oriented to geographical North and then backfilled with ice chips. The other receivers (CECE and KRIS) was installed within ~0.5 m deep pits in the rocky ground, oriented to geographical North, and then covered with rocky dirt. All instruments continuously sampled ground velocity at 200 Hz using a Quanterra digitizer and logged data to a solid state hard-drive. The data were retrieved the local summer of 2015.

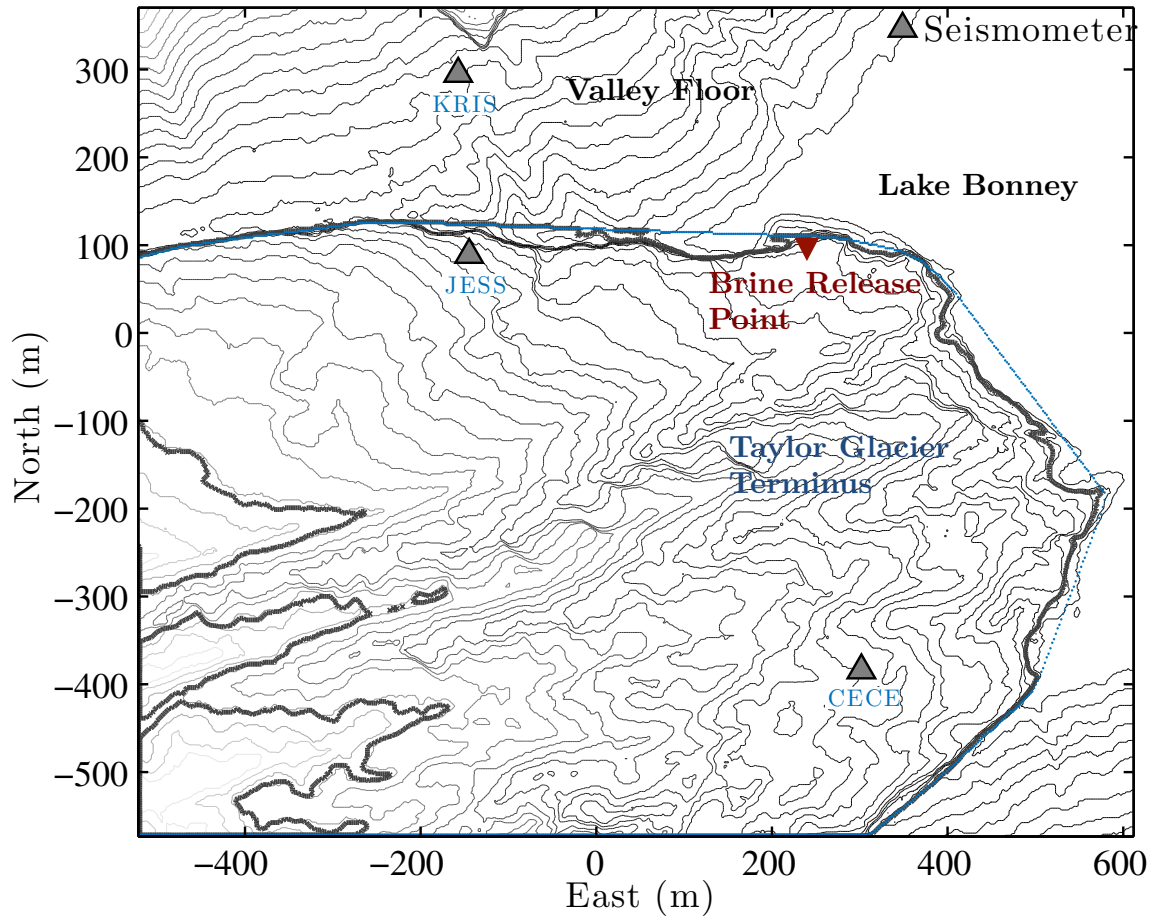


Figure 1 A 900m by 1100m overhead contour map of Taylor Glacier instrumented with 3 over-winter geophones. The glacier is interior to the blue curve; other geographical features are located.

May 13



Figure 2 Brine released from Taylor Glacier on May 13, 2014 (UTC).

3. Methods

To identify repeating collocated seismic sources (e.g., Figure 4), we processed our geophone data using a fully autonomous detection procedure. This procedure was implemented sequentially in the four following steps.

Collocated Events. DOY 133, Year 2014: 03:47:25 and 14:47:33

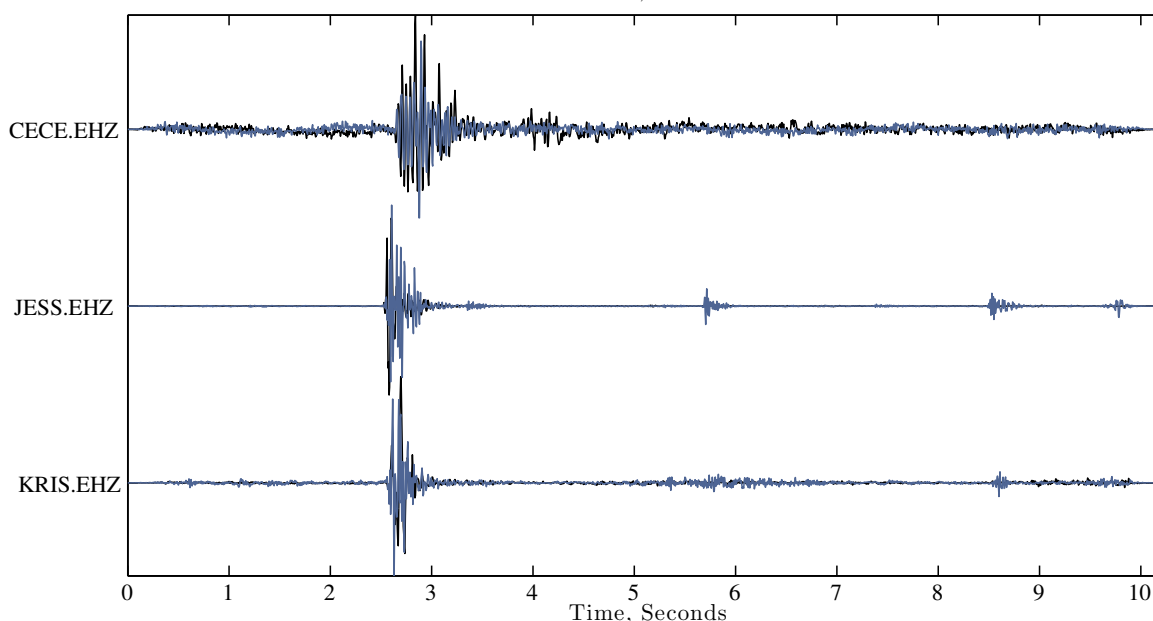


Figure 4 A pair of vertical channel multichannel seismic waveforms measuring ground velocity recorded on DOY 133, 2014 during a brine release event. The waveforms were recorded about 11 hours apart and show similar intra-event arrival times of equivalent waveform features and highly correlated waveform shapes. These attributes suggest that the waveforms originate from the same location and are triggered by similar focal mechanisms.

3.1 Seismic Event Identification

First, we identified individual seismic events by processing data from the vertical-channel of each geophone using a noise-adaptive, digital power detector. This detector computes a data statistic at each point in a geophone data stream by dividing an estimate of the sample variance within a leading data window by an estimate of the sample variance within a longer, following window i.e., the STA/LTA [Blandford, 1974]. To account for statistically correlated background noise that is common to glaciogenic environments (Figure 3),

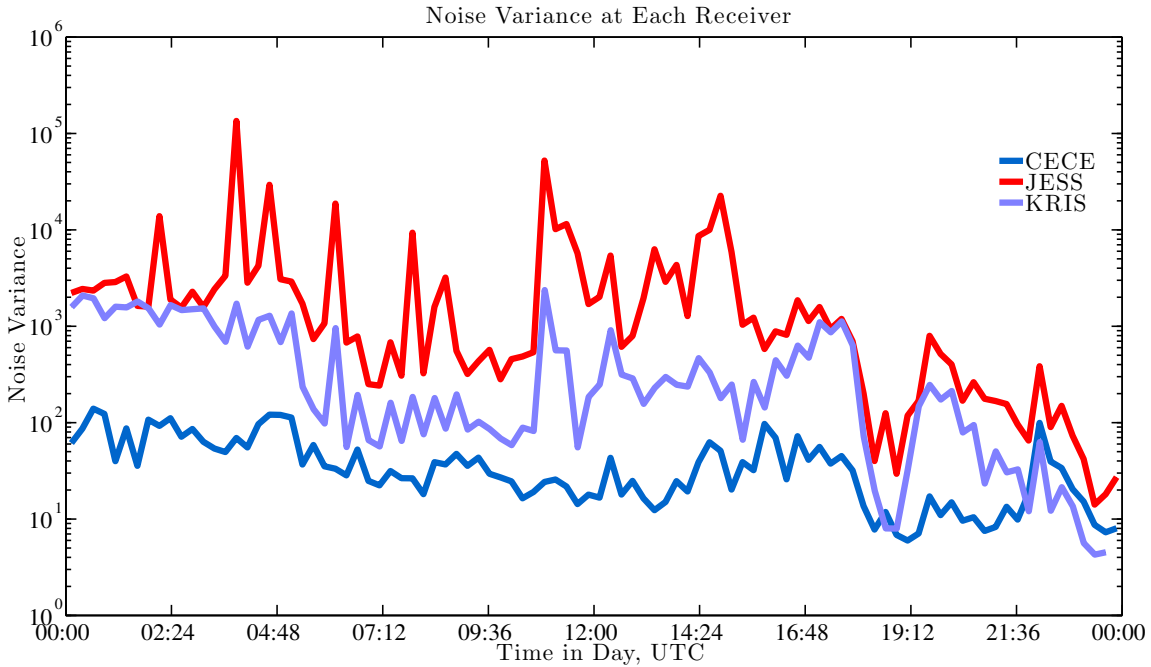


Figure 3 Noise variance estimates for each station in the network, computed in parallel with the power detector, after removing event detections. Note the vertical axis log scale. The noisiest station JESS is installed near the cliff face, where a substantial amount of melt and cliff face flexure occurs; KRIS is installed near the cliff face of the Rhone glacier; the quietest station (CECE) is installed farthest in-ice and away from any vertical ice surface.

we computed robust estimates for the degree-of-freedom parameters of the data statistic's F -distribution within each detection window (see Appendix A). These updated parameters enabled us to dynamically adjust the detector's event declaration threshold within each window and maintain a constant, acceptably low false-detection probability. We set this probability to 10^{-7} using the Neyman-Pearson decision rule [Kay, 1998; Chapter 7], so that waveforms with an SNR of ~ 10 dB had a 95% probability of being detected on a single geophone in average noise conditions. We document the computational form of the detection statistic, the decision rule threshold, and the density function's shaping parameters in Appendix A (see also [Carmichael *et al.*, 2015 a]). Results for a single, 15-minute recording period are illustrated in Figure 5.

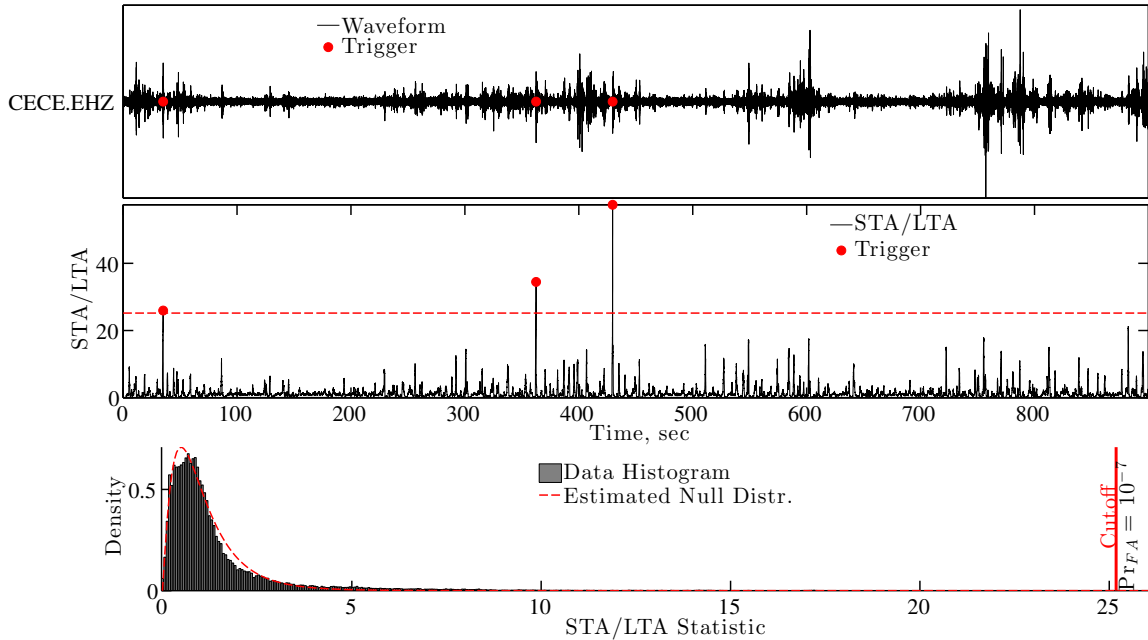


Figure 5 Power detector (STA/LTA) results as applied to 15 minutes of seismic data recorded at Taylor station CECE after local noon on DOY 133, which resulted in three, vertical channel detections. **Top:** Vertical channel seismic data bandpass filtered between 2.5 and 35 Hz. The red markers correspond to waveform detections and where the STA/LTA statistic exceeded the event declaration value; the other waveforms visually apparent in this panel are too emergent to trigger our detector. **Middle:** The STA/LTA statistic computed from the waveform data using a 0.65 sec (130 sample) short-term window and a 2.65 second (530 sample) long-term window; the red horizontal line shows the declaration threshold for a 10^{-7} false alarm rate (η). **Bottom:** The histogram (gray) of the STA/LTA statistic, superimposed with the hypothesized null distribution (red, dashed curve). The shaping parameters for the predicted curve were estimated from N_1 and N_2 (the distribution's degrees of freedom) and the red vertical line indicates the threshold η from the middle panel; both estimates were made using the data shown here.

3.2 Icequake Waveform Association

Next, waveforms detected on different geophones within a time interval less than the expected transit time of a shear wave across the network were identified as the same icequake (i.e., we performed waveform association). From these detections, we counted events that were large enough to be associated on all three geophones, and binned this count each hour to measure icequake seismicity (Figure 6). To quantify our confidence in this estimate, we identified time-windows where the predicted null (signal-absent) F -distributional curve for the STA/LTA statistic matched the data statistic's histogram with $\leq 20\%$ root-means-square error. These signals provided our best hourly estimate of the seismicity as well as a measure of confidence in our estimates (see also [Carmichael *et al.*, 2012; Carmichael *et al.*, 2015a]).

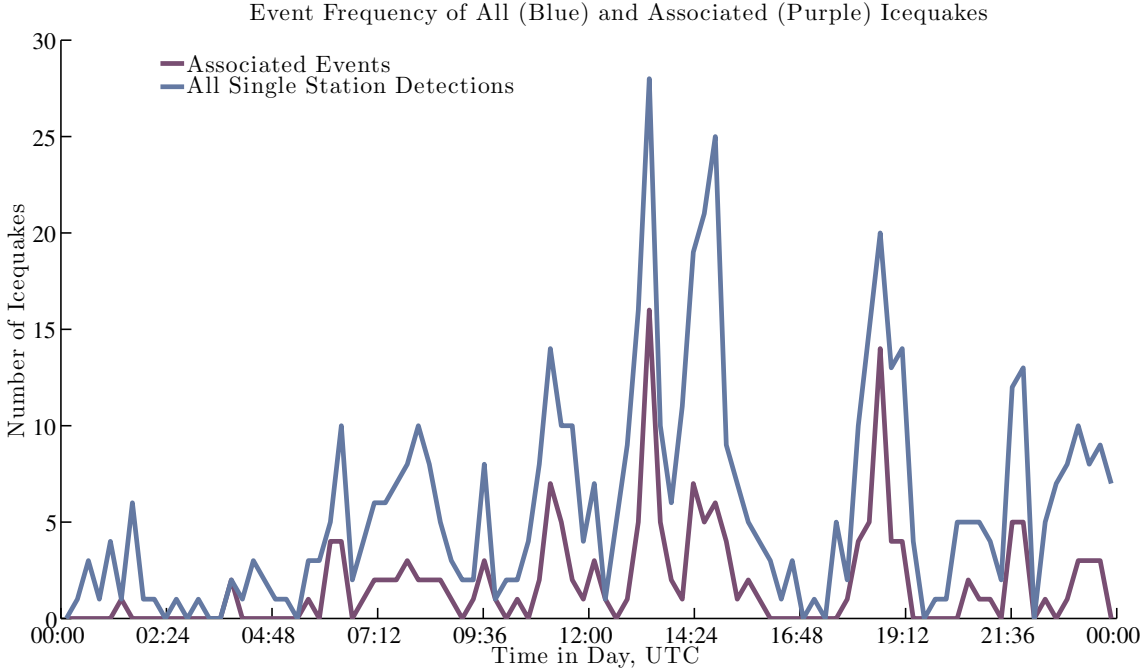


Figure 6 Power detector (STA/LTA) results for DOY 133, 2014. Seismic event frequency (seismicity) binned and counted into 15-minute intervals. The blue curve shows the total number of events that were detectable at one or more geophones. The purple curve shows seismicity for events large enough to register detections on all three receivers. These curves temporally correlate, and thereby suggest that strong events occur with weaker events.

3.3 Seismic Waveform Clustering

Third, we applied a hierarchical, complete-linkage clustering algorithm to all associated waveforms following Carmichael *et al.* [2012]. To perform this clustering, we first computed the correlation coefficient ρ between all possible pairs of associated multichannel waveforms, which were cut five seconds before their power-detected pick times and five seconds thereafter. A multichannel seismogram produced by a seismic source, sampled at interval Δt , is represented by a data matrix as follows:

$$\mathbf{W}(t) = [\mathbf{w}_1(t), \dots, \mathbf{w}_k(t), \dots, \mathbf{w}_N(t)], \text{ for } t = t_0, t_0 + \Delta t, \dots, t_0 + N\Delta t. \quad (1)$$

In Equation (1), matrix column $\mathbf{w}_k(t)$ is an N -sample seismogram from geophone k , recorded over T -seconds (10 sec here) from absolute reference time t_0 so that $\mathbf{w}_k(t_0 + n\Delta t)$ refers to sample n from geophone k . The correlation coefficient $\rho_{1,2}$ that quantifies the similarity between two different multi-channel signals $\mathbf{W}^{(1)}(t)$ and $\mathbf{W}^{(2)}(t)$, recorded from two different events, is derived from a maximum likelihood estimate [e.g., Harris, 1991; Carmichael *et al.*, 2015 b] given by:

$$\rho_{1,2} = \max_{\Delta t} \left\{ \frac{\text{tr}(\mathbf{W}^{(1)}(t + \Delta t)^T \mathbf{W}^{(2)}(t))}{\|\mathbf{W}^{(1)}(t)\|_F \|\mathbf{W}^{(2)}(t)\|_F} \right\}, \quad (6)$$

where $\|\mathbf{W}^{(k)}(t)\|_F$ is the matrix Frobenius norm and $\text{tr}(\mathbf{W}^{(k)}(t))$ is the matrix trace of $\mathbf{W}^{(k)}(t)$ ($k = 1, 2$). If a group of N multichannel waveforms correlated pair-wise above a threshold of $\rho_0 = 1/2$ so that every waveform correlated well with every other waveform in that group, we placed the waveforms into a cluster. We further constrained waveforms to be excluded from membership between clusters, e.g., no waveform could belong to more than one cluster. After our set assignment, waveforms within each cluster were then stacked (coherently averaged) to form a template waveform for a multichannel correlation detector. This process produced 20 distinct clusters for DOY 133, 2014 that each contained between seven and two multichannel waveforms with high mutual correlation. We then coherently averaged the waveforms composing each cluster to construct a single waveform representative of the signals therein.

3.4 Waveform Correlation Detection

To search for similar waveforms not initially identified with our power detector and assigned to a cluster, we implemented a multichannel correlation detector. Multichannel correlation detectors compare template waveforms recorded from a given reference event with noisy data to identify similarly shaped “target” waveforms using a sample correlation coefficient. This coefficient generalizes the correlation $s(x)$ between pairs of single-channel waveforms to pairs of multichannel waveforms that represent measurements of seismic velocity recorded by a clock-synchronized, L -element seismic network [Harris, 1991; Gibbons and Ringdal, 2006]. These detectors effectively identify sources known as “seismic multiplets”, which comprise clusters of variable-magnitude earthquakes (or icequakes) that reoccur as distinct events, have similar hypocenters, and produce highly correlated seismograms [e.g., Moriya *et al.*, 2003]. Our correlation detector tests the correlation between a multichannel template waveform $\mathbf{W}(t)$ (taken from a cluster) and commensurate data stream matrix $\mathbf{X}(t)$ against a computed threshold η according to the following decision rule:

	$s(x) = \frac{\text{tr}(\mathbf{W}(t + \Delta t)^T \mathbf{X}(t))}{\ \mathbf{W}(t + \Delta t)\ _F \ \mathbf{X}(t)\ _F} \begin{matrix} H_1 \\ > \\ < \\ H_0 \end{matrix} \eta$	(2)
--	---	-----

where $\|\mathbf{W}(t)\|_F$ is the matrix Frobenius norm and $\text{tr}(\mathbf{W}(t))$ is the matrix trace of $\mathbf{W}(t)$ ($k = 1, 2$), as before. The hypothesis H_0 below the conditional inequality signifies that $\mathbf{X}(t)$ consists of Gaussian noise ($\mathbf{X}(t) = \mathbf{N}(t)$) when $s(x) < \eta$; the hypothesis H_1 then signifies that $\mathbf{X}(t)$ consists of a scaled-copy of the template waveform $\mathbf{W}(t)$ buried in Gaussian noise ($\mathbf{X}(t) = A \cdot \mathbf{W}(t) + \mathbf{N}(t)$) if $s(x) > \eta$, where A is a scalar. However, noisy non-target waveforms originating from background seismicity may also be recorded and misdetected. Such false-detections occur if a signal within the data stream is sufficiently coherent with the template waveform that the correlation $s(x)$ exceeds the prescribed threshold for event declaration (η in Equation 2). In practice, this threshold so high that white noise has a very low chance of generating false detections, and therefore spuriously high correlation values are usually induced by nearly monochromatic noise or

non-target seismicity. Alternatively, target waveforms that are (nearly) collocated with the template source may still generate lower-than-predicted cross-correlation ($s(x) < 1$) if the underlying signals exhibit incoherence with the template signal due to differences in radiation pattern.

When only subsets of network geophones were logging data in a given period, only matrix columns containing operational stations were compared. We only included event detections where $s(x) > 1/2$ for analyses (Figures 7 a,b; red lines) after visual inspection suggested that waveforms sharing lower correlation likely had dissimilar sources or focal mechanisms, or that the waveform SNR was too low for interpretation. This correlation threshold gave a negligible false-alarm on noise probability, as determined by the correlation-coefficient's empirical null distribution [e.g., Weichecki-Vergara, 2001; Carmichael, 2013] parameterized by a mean effective degrees of freedom parameter:

	$\int_{1/2}^{\infty} f_s(s(x); H_1) dS \sim 10^{-200}$	(3)
--	--	-----

This indicates that background noise has effectively zero probability of triggering our detector, so that only partially coherent background seismicity from other (non-target) earthquakes (or icequakes) likely generate false detections (Figures 7 a,b; bottom panels)

Having established our detector thresholds, we processed all nine channels (three stations) of our data with each cluster-template. This processing identified 140 additional waveforms (Figure 8) among 14 different clusters (multiplet sequences) that satisfied each respective correlation detector's decision rule (e.g., Equation 2).

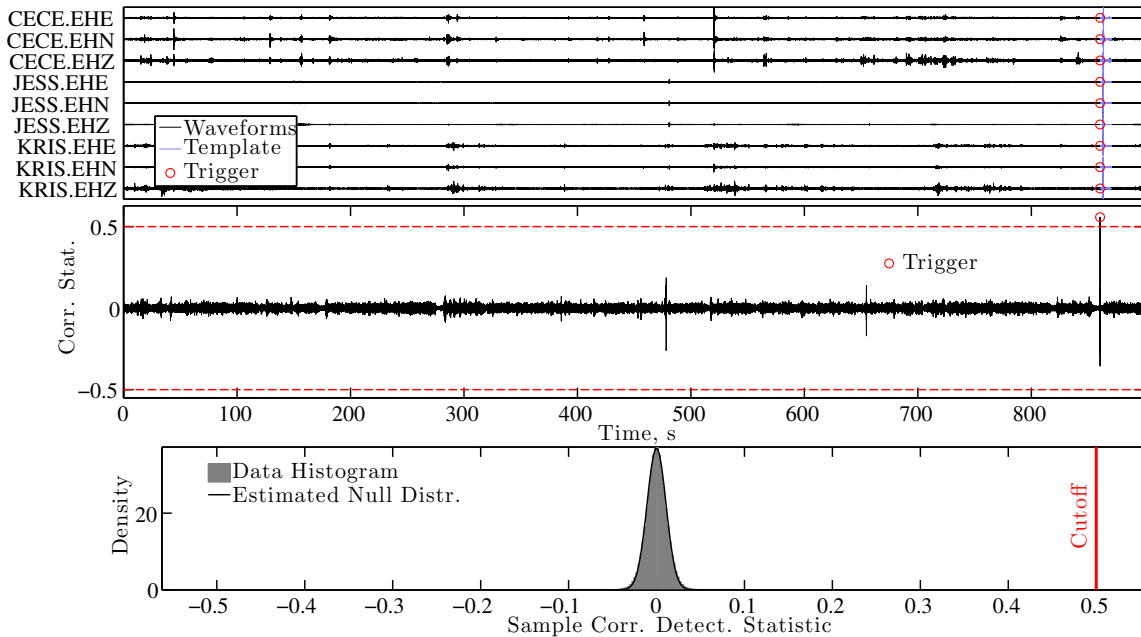


Figure 6a An example of processing data recorded at the Taylor network in 2014 with a correlation detector that includes a template selected from the coherent waveform stack

of the most populous cluster. **Top:** A nine-channel data stream (black) recorded on DOY 133, 2014 during a brine release episode. The purple data segment shows the template waveforms superimposed on the black data-stream and temporally aligned at the peak correlation value. The red markers indicate the time of an event-declaration. **Middle:** The correlation statistic $s(\mathbf{x})$ computed by scanning the template waveform against the data stream at top. The red, horizontal line indicates the threshold for event declaration, determined by an effectively zero false alarm on noise probability constraint, as computed from the signal-absent distribution using the Neyman Pearson criteria. **Bottom:** The histogram computed from the correlation statistic time series (gray) superimposed with the theoretical null distribution (black curve) shaped by an effective degrees of freedom parameter N_E . The red vertical line shows the threshold for event declaration, consistent with an effectively zero right-tail probability as computed from the black curve. The theoretical distribution fits the observed histogram with a 6% relative error.

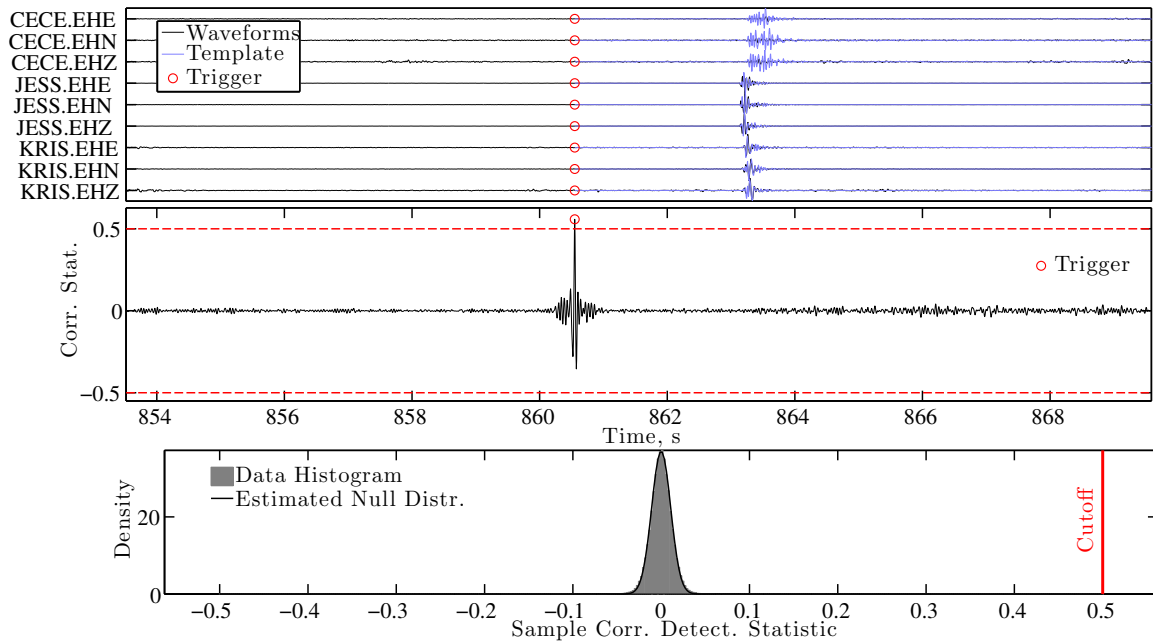


Figure 6b A time-limited view of Figure 6a. The top plot now shows the template waveform (purple) superimposed on top of the target data (black). The middle plot shows the correlogram near peak correlation, well above background correlation values.

4.1 Results and Conclusions

We have analyzed seismic data recorded on Taylor Glacier, ANT during a single day with a documented brine release episode (DOY 133, 2014). Our analyses focused on quantifying background seismic activity recorded by a small, three-element triaxial seismic network and identifying similar waveforms ostensibly triggered by spatially localized, repeating brittle deformation of glacial ice. Our fully autonomous signal detection methodology (1) identified seismic events using a noise-adaptive power detector based on statistically significant seismic waveforms; (2) associated waveforms that were observable on three or more station; (3) clustered associated waveforms with a

complete linkage clustering algorithm designed for glacial ice to identify seismic multiplets; (4) coherently stacked all members of each cluster population to form a multiplet template; and (5) used these templates in a nine channel correlation detector to identify additional, repeating seismic events with similar waveforms and source locations. Applied to our dataset, we identified 127 network-associated seismic events on DOY 133, 2014 that were detectable on all three stations (Figure 6, purple curve) and observed no false alarms on background noise. This seismic event population comprised 53 events (~40% of the total, power-detected event population) that could be assigned to 20 unique multiplet sequences (clusters). To test whether the members of the three most populous multiplet populations were glaciogenic, we compared observed p -wave arrival times for these events with forward modeled travel times between each receiver for several synthetic sources. Based on these relative arrival times, we conclude that the observed sources could not be North of station JESS and must be glaciogenic and are therefore icequakes.

Having established these multiplets as likely icequakes, we found 140 additional waveforms with membership to 14 of these 20 clusters by using the mean waveform from each icequake cluster as a template (Figures 7 a,b; purple traces) within a nine-channel correlation detector. Repeating seismic events therefore composed a comparable percentage (> 55%) of the total detected, icequake population (Figure 8). The most populous of the resultant clusters included 27 distinct seismic events. The waveforms in this cluster were highly correlated, and showed an average template-waveform correlation coefficient $\overline{s(x)} \cong 0.64$ and peak correlation value of $\max\{s(x)\} \cong 0.87$ (Figure 9, left panel). Some of this observed variability resulted from additional signal phases that may be attributed to Rayleigh waves, or closely spaced secondary events (Figure 9; waveforms following main phase in right panel at ~3.7 sec). The remaining variability reflects lower signal-to-noise characteristics and interference from narrowband noise that may be induced by thermal stresses in the shallow ice. Cumulatively, these highly correlated waveforms represent activation of repeatable seismic sources, like large englacial fractures, that were spatially localized and had identical (or nearly so) focal mechanisms. While these results are limited to one day, they may be applied to a longer data set to include background seismicity and additional brine release episodes. If additional work demonstrates that such icequakes indicate brine release, we suggest applying our method to an autonomous seismic monitoring program of Blood Falls.

Event Frequency of All (Blue) and Multiplet (All) Icequakes

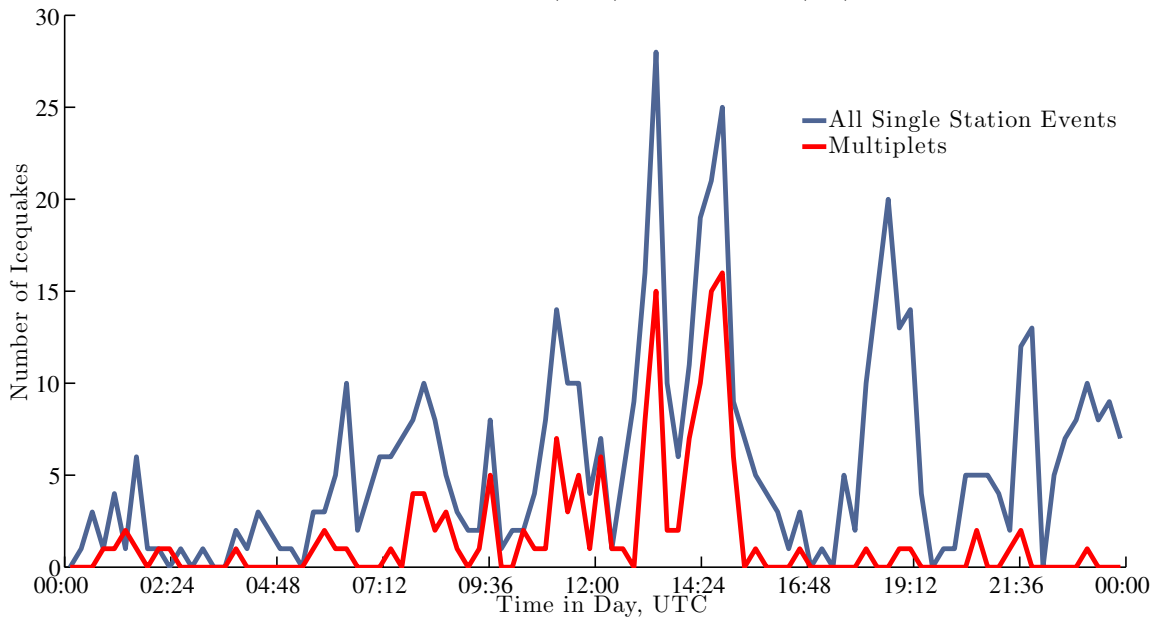


Figure 8: Seismicity from single-station event detections on DOY 133, 2014 compared against multiplets identified with a correlation detector. In both cases, seismicity is counted and binned into 15-minute intervals. The blue curve shows the total number of events that were detectable on at one or more geophones. The red curve shows timing of events that correlated with any cluster template waveform. The timing of multiplets peak coincidentally with maxima in seismicity.

4.2 Future Work

Our future work will be devoted to two primary tasks. The first task will be processing our entire data set using the method illustrated here, so that (a) days that include brine release can be compared against each other for location, timing and magnitude and (b) days that include no observed brine release episodes can be compared against ambient, background seismicity at Taylor Glacier. Our second task will be locating these repeating events. While our network comprises only three receivers compared to four unknown hypocentral parameters, we can eliminate time and fix depth in applying hypocentral regression. We can fix depth since our network has relatively poor depth resolution, and any parameter estimate will likely be unreliable. We can eliminate time arithmetically by using a centered and scaled version of the regression equations (Equation 2 of [Carmichael *et al.*, 2012]). We propose to first locate the template waveform's source (or the detected waveform with the highest SNR), and thereafter locate the events it identifies as similar. The mean hypocentral location between the template and following (correlation detected) events will then provide a lower-variance estimate for spatially localized multiplet source.

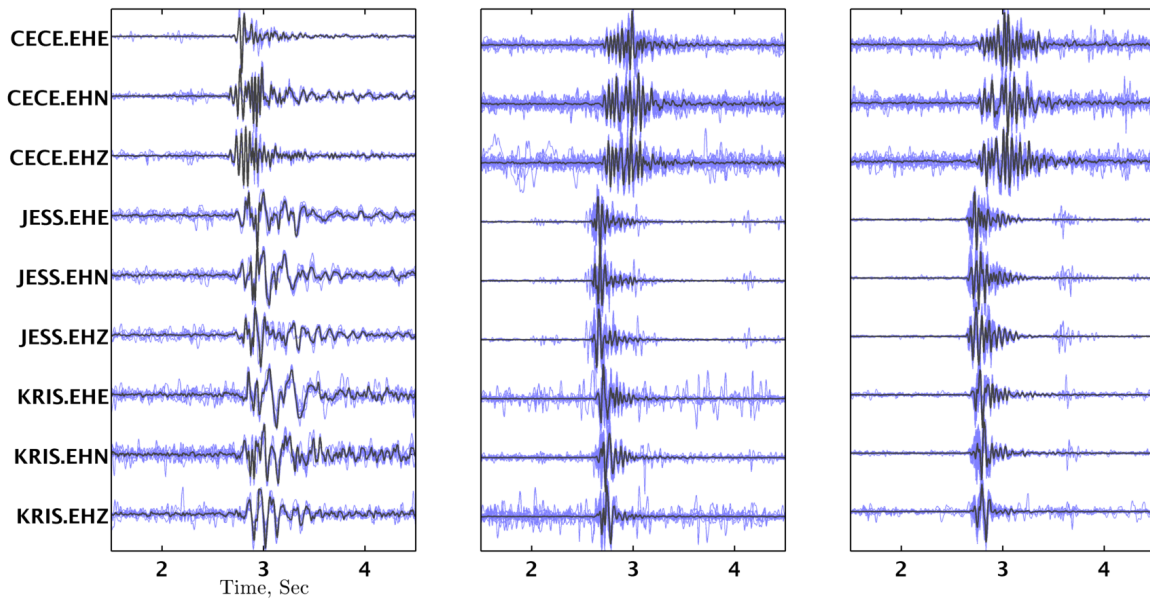


Figure 9 Correlation detected waveforms for three separate multiplet sequences. In each panel, the purple traces show waveforms identified by a correlation detector template (black) that was obtained by coherently stacking associated waveforms within a cluster. The left most panel shows waveforms associated with the most populous cluster, which contained 7 events; the correlation detector identified an additional 20 icequake events that triggered similar waveforms (27 purple waveforms plotted). The sources producing this multiplet sequence appear to be spatially separated from the sources producing the multiplets in the middle and right panel, based on the relative arrival times of the waveforms at each receiver.

Acknowledgments, Researcher Biographies

Data collection was led by Dr. Erin Pettit of the University of Alaska Fairbanks (UAF) under NSF grant #1144177 Collaborative Research: MIDGE: Minimally Invasive Direct Glacial Exploration of Biogeochemistry, Hydrology and Glaciology of Blood Falls, McMurdo Dry Valleys. Christina Carr, is a geophysics PhD student at the University of Alaska (Fairbanks) analyzing several of the geophysical datasets discussed herein. Joshua D Carmichael is a post-doctoral researcher with EES-17 at Los Alamos National Laboratory.

References and Further Reading

- Blandford, R. R., (1974), An Automatic Event Detector At The Tonto Forest Seismic Observatory, *Geophysics*, 39(5), 633-643.
- Carmichael, J. D., I. Joughin, M. D. Behn, S. Das, M. A. King, L. Stevens, and D. Lizarralde (2015), Seismicity on the Western Greenland Ice Sheet: Surface Fracture in the Vicinity of Active Moulins, *J. Geophys. Res. Earth Surf.*, 120, doi:[10.1002/2014JF003398](https://doi.org/10.1002/2014JF003398).

- 358 Carmichael, J.D., Nemzek, R., Arrowsmith S., and Sentz, K. (2015), Detecting Weak
359 Explosions at Local Distances by Fusing Multiple Geophysical Phenomenologies,
360 *Geophysical Journal International*, (In Review; Manuscript ID GJI-S-15-0027)
- 361 Carmichael, J. D., E. C. Pettit, M. Hoffman, A. Fountain, and B. Hallet (2012), Seismic
362 multiplet response triggered by melt at Blood Falls, Taylor Glacier, Antarctica, *J.*
363 *Geophys. Res. -Earth Surf.*, 117, F03004, doi: 10.1029/2011JF002221.
- 364 Carmichael, Joshua D. *Melt-Triggered Seismic Response in Hydraulically-Active Polar*
365 *Ice: Observations and Methods*. PhD thesis, University of Washington, 2013, uri:
366 <http://hdl.handle.net/1773/25007>
- 367 Gibbons, S. J. and F. Ringdal (2006), The detection of low magnitude seismic events
368 using array-based waveform correlation, *Geophysical Journal International*, 165(1),
369 149-166, doi: 10.1111/j.1365-246X.2006.02865.x.
- 370 Harris, D. B. (1989). *Characterizing source regions with signal subspace methods:*
371 *theory and computational methods* (No. UCID-21848). Lawrence Livermore National
372 Lab., CA (USA).
373
- 374 Harris, D. B. (1991). A waveform correlation method for identifying quarry explosions.
375 *Bulletin of the Seismological Society of America*, 81(6), 2395-2418.
- 376 Kay, S. M., (1998), *Fundamentals of Statistical Signal Processing: Volume II*, Prentice-
377 Hall PTR, Englewood Cliffs, N.J.
- 378 Moriya, Hirokazu, Hiroaki Niitsuma, and Roy Baria. Multiplet-clustering analysis reveals
379 structural details within the seismic cloud at the Soultz geothermal field, France.
380 *Bulletin of the Seismological Society of America* 93.4 (2003): 1606-1620, doi:
381 10.1785/0120020072
- 382 Weichecki-Vergara, S., H. L. Gray, and W. A. Woodward (2001), Statistical
383 development in support of CTBT monitoring, Tech. Rep. DTRA-TR-00-22, Southern
384 Methodist Univ., Dallas, Texas

385

Appendix A: Power Detectors

Icequakes must have sufficiently large magnitudes to generate ice motion that is detectable by the geophones within a network. Weaker or remote icequakes will produce smaller displacement amplitudes at the source that are statistically more difficult to distinguish from the expected amplitude of background noise recorded by geophones in the far field. To discriminate icequakes from such noise, a power detector evaluates a statistic z_k that is computed from a ratio of short-term and long-term averages (STA/LTA) of signal power [Blandford, 1974]. This statistic is derivable from a generalized likelihood ratio test [Carmichael, 2013] and is expressed at sample k , within a detection window containing statistically stationary noise, as:

$$z_k = \left(\frac{1}{S} \sum_{n=k}^{n=k+S-1} \left(\frac{x_n}{\sigma} \right)^2 \right) \div \left(\frac{1}{L} \sum_{n=k-L+1}^{n=k} \left(\frac{x_n}{\sigma} \right)^2 \right) \quad (\text{A.1})$$

where x_k is sample k of the observed seismogram, S is the leading, short window length in samples, L is the following long window length in samples, and σ is the standard deviation of background noise in the current detection window; while z_k is independent of σ , we have retained it here for clarity.

The statistic z_k has two distinct probability distribution functions; one applicable to the case of absent signal (a central F distribution), and one applicable to the case of present signal (a non-central F distribution); their analytical forms are described in several places (e.g., Kay, 1998; Carmichael 2013). Deciding an icequake has occurred is equivalent to choosing the distribution function that explains the measured value of the STA/LTA statistic at a prescribed probability. The signal-present distribution is parameterized by a so-called non-centrality parameter λ that is proportional to the waveform signal-to-noise ratio (SNR), which is zero for the signal absent case. This parameter is defined by:

$$\lambda = \sum_{k=1}^S \left(\frac{A_k}{\sigma} \right)^2. \quad (\text{A.2})$$

In Equation A.2, A_k is the true (noise-free) waveform amplitude at sample k , which is related to the noise-contaminated data through $x_k = A_k + n_k$, where n_k is a sample of zero-mean background noise with standard deviation σ^2 . Increasing values of λ (relative to zero) result in decreased overlap between the signal-present and signal-absent distribution and makes correctly discriminating between noise and an icequake more probable. A 0.95 probability of detecting an icequake at sample k that produces parameter λ is then obtained by integrating the probability density function over the detector threshold η consistent with a 10^{-7} detection probability:

$$0.95 = \int_{\eta}^{\infty} f_{z_k}(z_k; \lambda, N_1, N_2) dz_k \quad (\text{A.3})$$

where:

$$10^{-7} = \int_{\eta}^{\infty} f_{z_k}(z_k; \lambda = 0, N_1, N_2) dz_k$$

422

423 In Equation A.3, $f_{z_k}(z_k; \lambda, N_1, N_2)$ is the signal-present F distribution, and $f_{z_k}(z_k; \lambda =$
 424 $0, N_1, N_2)$ is the signal absent F distribution (Figure A.1, bottom); each are parameterized
 425 by two degree-of-freedom parameters N_1 and N_2 that are respectively equal to S and L for
 426 white noise, but substantially less for real, temporally correlated noise. We estimate these
 427 parameters from our data using the mean and variance of the STA/LTA statistic:
 428

$$\begin{aligned} E(z) &= \frac{N_2}{N_2 - 2} \\ \text{var}(z) &= \frac{2N_2^2(N_1 + N_2 - 2)}{N_1(N_2 - 2)^2(N_2 - 4)} \end{aligned} \tag{A.4}$$

429

430 Using Equation A.4, we computed the sample mean and sample variance in place of the
 431 true mean $E(z)$ and variance $\text{var}(z)$ within each one-hour detection window using
 432 thousands of samples of z_k , and then solved for N_1 and N_2 .